Available online at www.sciencedirect.com

ScienceDirect

Ceramics International 39 (2013) 8925–8931

CERAMICS INTERNATIONAL

www.elsevier.com/locate/ceramint

Silver and fluoride doped hydroxyapatites: Investigation by microstructure, mechanical and antibacterial properties

Mustafa Turkoz[a], Aykan Onur Atilla[b], Zafer Evis[c,*]

[a]*Department of Physics, Kirikkale University, Kirikkale 71450, Turkey*
[b]*Kecioren Osmanlı Dental Center, Ankara 06010, Turkey*
[c]*Department of Engineering Sciences, Middle East Technical University, Ankara 06800, Turkey*

Received 28 March 2013; received in revised form 23 April 2013; accepted 24 April 2013
Available online 10 May 2013

Abstract

Hydroxyapatite co-doped with Ag^+ and F^- ions was synthesized by the precipitation method and sintered at 1100 °C for 1 h. Samples were characterized by density, X-ray diffraction, Fourier transform infrared spectroscopy, Raman spectroscopy, and scanning electron microscopy to investigate their microstructure, phase formation and bonding characteristics. Moreover, samples were also characterized by microhardness and antibacterial tests. Small amount of dopings resulted in high densities and fine grain microstructures. In most of the samples, hydroxyapatite was the main phase with a minor amount of β-TCP. Presence of fluoride and small amount of TCP was verified with all characteristic FTIR bands of hydroxyapatite for most of the samples. Compared to the pure hydroxyapatites, much higher microhardness values were measured in samples co-doped with Ag^+ and F^- ions. Antibacterial activity of the materials related to *Escherichia coli* was also observed in hydroxyapatite samples with high amount of Ag^+ ions.

Keywords: Hydroxyapatite; Silver; Fluoride; Microstructure; *Escherichia coli*

1. Introduction

Hydroxyapatite ($Ca_{10}(PO_4)_6(OH)_2$) (HA) is the most biocompatible and bio-active ceramic among the other calcium phosphates (CaP) [1,2]. Presence of secondary phases, surface characteristics, grain size, and amount of porosity in HA affect its biological properties [3–7]. Although HA is highly osteoconductive, its antibacterial resistance is very limited. For this reason, Ag^+ ions were introduced into HA to improve its antibacterial characteristics [8–11].

Ag^+ doped HAs were previously synthesized by the precipitation method and sintered at various temperatures [11,12]. It was presented that presence of Ag^+ in HAs and CaPs showed improved antibacterial activities [9,13]. Moreover, co-doping of Ag^+ and Cu^{2+} in HA also improved its antibacterial performance [14]. It was shown that HA doped with Ag^+ and Cu^{2+} ions resulted in an increase in its crystals along the *c*-axis with a platelet morphology [14]. Ag^+ (x) doped HAs ($0.5 \geq x \geq 0.3$, $0.5 \geq x \geq 0.03$, and $0.04 \geq x \geq 0.002$) with the formula of $Ca_{10-x}Ag_x(PO_4)_6(OH)_2$ showed statistically improved cell viability and antibacterial activity than pure HA [8,15,16]. HAs doped with high amount of Ag^+ ions had lower flexural strength and modulus values than pure HA or HA doped with small amount of Ag^+ ions [17]. Nanocomposite spheres of HA with Ag particles related to their electrostatic effect were synthesized successfully [18].

Ag^+ ions were doped into the plasma sprayed HA coatings on titanium susbstrates to improve their antibacterial characteristics [19]. It was presented that Ag_2O doped HA coatings showed improved activities against to *Pseudomonas aeruginosa* [19]. Sputtering and co-sputtering methods were used to coat Ag^+ containing HA (thin films) on Ti substrate to get an improvement against to bacterial activities [20,21].

In a study regarding HA and Ag–TiO_2 composites, photocatalytic properties of HA and 1 wt% Ag–TiO_2 composite system showed a 100% reduction in *Escherichia coli* (*E. coli*) activity within 2 min [10]. Moreover, resorbable CaP cements doped with Ag^+ ions showed a controlled resorbable behavior with a possibility to inhibit bacterial infections related to

---

[*] Corresponding author. Tel.: +90 312 2104450; fax: +90 312 2104462.
E-mail address: evis@metu.edu.tr (Z. Evis).

0272-8842/$ - see front matter © 2013 Elsevier Ltd and Techna Group S.r.l. All rights reserved.
http://dx.doi.org/10.1016/j.ceramint.2013.04.088

implantation steps [22]. Treatment of HA with silver diamine fluoride resulted in formation of silver nanoparticles on HA surface [23]. Moreover, silver nitrate reacted with HA to form Ag_3PO_4 [23]. Mechanical properties of PCL–HA–Ag composite nanofibers were higher than those of PCL–HA composite [24]. HA with Ag^+ loaded zirconium phosphate particles showed a resistance to bacterial activity of *E. coli* in the presence of Cl^- ion [25,26].

HA doped with F^- ions showed low solubility, high biocompatibility, improved osteoblast proliferation and differentiation, improved thermal and chemical stability when compared with pure HA [27–34]. Amount of F^- ions in HA should be adjusted to an optimum value because it will cause some disadvantages in terms of cell activities when its concentration is above a critical level [35]. Nanostructured fluorapatite with spheroidal shape can be obtained with a mechanochemical synthesis process and thermal treatment at a low temperature such as 600 °C [36]. For $Ca_{10}(PO_4)_6(OH)_{2-x}F_x$, smallest grain size was obtained when x was equal to 0.4 when compared with other compositions of the hydroxy-fluorapatite in which x was equal to 0, 0.4, 0.8, 1.2, 1.6, and 2 [37]. Moreover, a decrease in hardness, elastic modulus, and brittleness was observed with higher F^- content in hydroxy-fluorapatites because of low density values for higher F^- content in them [38]. For fluorapatites, highest density was obtained after the sintering at 890 °C in the sintering range from 640 to 1365 °C [39]. Above 1180 °C, formation of a liquid phase was reported for fluorapatite [39].

Although doping of Ag^+ ions into HA was previously studied, co-doping of Ag^+ and F^- ions into HA was not previously studied. HAs co-doped with Ag^+ and F^- ions were synthesized by the precipitation method and sintered at 1100 °C for 1 h for the first time for antibacterial purposes. Samples were characterized by structural (density, X-ray diffraction (XRD), Fourier transform infrared spectroscopy (FTIR), Raman spectroscopy, and scanning electron microscopy (SEM)), microhardness, and antibacterial with *E. coli* methods.

2. Materials and methods

The precursors used to synthesize pure HA were calcium nitrate tetrahydrate ($Ca(NO_3)_2 \cdot 4H_2O$) and diammonium hydrogen phosphate ($(NH_4)_2HPO_4$) [40]. For doped samples, ammonium fluoride (NH_4F) and silver nitrate ($Ag(NO_3)$) were added into the HAs for F^- and Ag^+ dopings, respectively. The pH adjustment was made by addition of ammonia solution (NH_4OH) into the solution. Prepared solution was then stirred for precipitation for 24 h. After 24 h, the stirred mixture was filtered to obtain a wet cake. Then it was dried overnight at 200 °C to remove excess water and ammonia. Dried samples were sintered at 1100 °C for 1 h. It was reported that the optimum sintering temperature for HA is 1100 °C for 1 h to obtain pore-free, single-phase, translucent HA [41]. For every 10 mol of $Ca(NO_3)_2 \cdot 4H_2O$, 0.05, 0.1 and 0.2 mol of $Ag(NO_3)$ were incorporated into samples of 0.5Ag, 1Ag, and 2Ag, respectively. Moreover, 0.1, 0.2 and 0.3 mol of NH_4F was used for the samples of 1F, 2F, and 3F, respectively. Moreover, 0.05, 0.1 and 0.2 mol of $Ag(NO_3)$ and 0.1 mol of NH_4F were used for the preparation of 0.5Ag1F, 1Ag1F and 2Ag1F samples, respectively. Furthermore, samples of 5Ag, 10Ag, 5Ag1F, and 10Ag1F were synthesized for antibacterial study.

Densities of the sintered samples were determined by the Archimedes method. Relative density of the materials was calculated by dividing the measured density with theoretical density of pure HA (3.156 g/cm^3) [42].

Sintered samples were characterized by XRD with a Bruker D8 Advance diffractometer using Cu-Kα radiation at 40 kV and 40 mA with a range from 10° to 80° with a scanning speed of 1.0 deg/min. Phases present in the samples were determined by comparing the experimental XRD pattern to standard International Center for Diffraction Data (ICDD) files.

Pure and doped HA tables were used for FTIR measurement. They were mixed with potassium bromide (KBr) in a weight ratio of 1–300. The powders were cold pressed to obtain transparent pellets. Then, the spectra were recorded over the range of 4000–400 cm^{-1} with a Bruker Bertex 70 FTIR equipment. Samples were also analyzed with a Raman shift with 532 nm and the Raman spectra were recorded over the range of 4000–400 cm^{-1} (Bruker Optics Senterra).

The morphology of the samples was analyzed by SEM (Joel JSM 5600). SEM images were used to determine the average grain size of the samples.

Micro-hardness test was applied to the samples with a Shimadzu HMV-2 Vickers micro-hardness tester. All the sintered samples were embedded into epoxy molds, polished and tested by the microhardness tester. A load of 1.961 N was applied on the samples by a diamond indenter for 20 s. 20 measurements were performed on each sample. The formula (Eq. (1)) used for the calculation is as follows:

$$HV = 0.001854\frac{P}{d^2} \tag{1}$$

where HV: Vickers hardness (GPa); P: applied load (N); and d: diagonal indent length (mm).

E. coli cultures were seeded to 10 ml of nutrient broth medium. They were left to incubation at 37 °C for 24 h. Grown microorganisms were compared with Mcfarland turbidimetry tubes in the medium. Bacteria count was determined as 2700×10^6/ml and 100 ml of medium (*E. coli*) was obtained in the tube. Nutrient agar solid mediums were seeded. Samples prepared as 1 mg/ml in concentration, were soaked on discs left in a 10 μl of medium. They were incubated at 37 °C for 24 h. Tetracycline antibiotic discs were used for *E. coli* as a control. After the incubation, zone diameters were determined.

3. Results and discussion

Densities of the samples sintered at 1100 °C for 1 h are presented in Table 1. All of the samples showed relative densities more than 91%. Pure HA had a relative density of 97.01%. Moreover, increasing the F^- ion amount from 1F to 3F resulted in a decrease in the densities. Moreover, doping small amount of Ag^+ ion (0.5Ag) into HA increased the

Table 1
Density of the samples after sintering at 1100 °C for 1 h.

Sample ID	Sintered density (g/cm^3)	Relative density (%)
Pure	3.0617	97.01
1F	3.0325	96.08
2F	3.0733	97.38
3F	2.9353	93.01
0.5Ag	3.0883	97.85
1Ag	3.0303	96.02
2Ag	3.0221	95.76
0.5Ag1F	3.0408	96.35
1Ag1F	2.9227	92.61
2Ag1F	2.8771	91.16

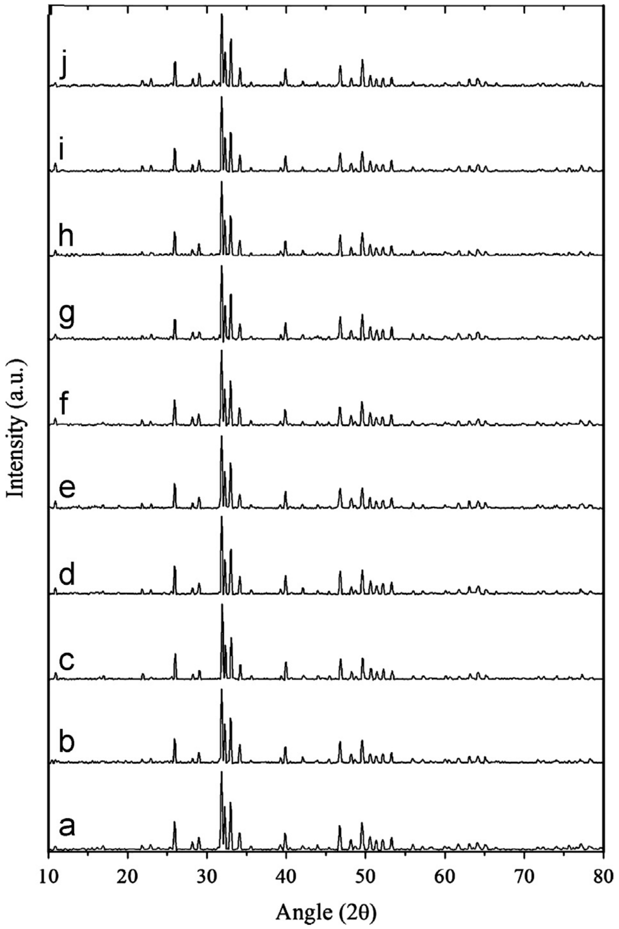

Fig. 1. XRD patterns of samples sintered at 1100 °C for 1 h: (a) pure HA; (b) 1F; (c) 2F; (d) 3F; (e) 0.5Ag; (f) 1Ag; (g) 2Ag; (h) 0.5Ag1F; (i) 1Ag1F; and (j) 2Ag1F.

density to 97.85%. However, further increase to 1Ag and 2Ag decreased the density values. Similar trend was also observed for 0.5Ag1F, 1Ag1F, and 2Ag1F samples.

XRD data of the samples sintered at 1100 °C for 1 h are presented in Fig. 1. Main phase in all of the samples was identified to be HA (ICDD #09-0432). XRD main peak of the samples was located at 2-theta (2θ) angle of around 31.84 which is close to main peak ($2\theta=31.77$) of pure HA. Although most of the samples were pure HA, there was a minor secondary phase for the samples of 1Ag, 2Ag, 1Ag1F, and 2Ag1F (Fig. 1f, g, i, and j). The extra peak for each of these samples was observed at 2θ angle of 31.00. It was attributed to the β-tri-calcium-phosphate (β-TCP). This secondary phase was matched with standard β-TCP with a reference of ICDD #09-0169. This probably occurred due to the higher amount of dopants which may further result in an effect on the decomposition of HA.

Metallic Ag phase was previously observed for 1 wt% Ag and 5 at% Ag doped HAs [10,16]. Moreover, in another study, Ag_2O phase was observed in Ag^+ doped HAs [19]. In the samples of $Ca_{10-x}Ag_x(PO_4)_6(OH)_2$ when x was between 0.3 and 0.5, HA and small amounts of α-TCP were observed after the sintering at 1200 °C and amount of α-TCP was increased with higher Ag^+ doping and no silver oxide was observed [8]. Moreover, it was previously stated that Ag^+ ion substitution for Ca^{2+} in HA is possible when it is less than 4 at% [43]. Other than HA and small amount of β-TCP phases, other phases were not observed for the samples synthesized in this study. This showed that Ag^+ ions were successfully incorporated into HA.

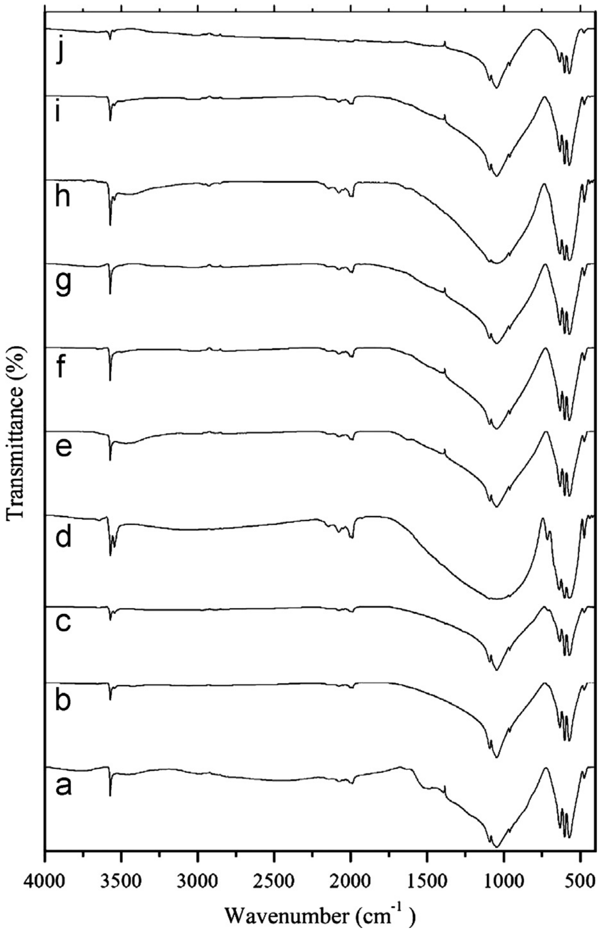

Fig. 2. FTIR spectra of samples sintered at 1100 °C for 1 h: (a) pure HA; (b) 1F; (c) 2F; (d) 3F; (e) 0.5Ag; (f) 1Ag; (g) 2Ag; (h) 0.5Ag1F; (i) 1Ag1F; and (j) 2Ag1F.

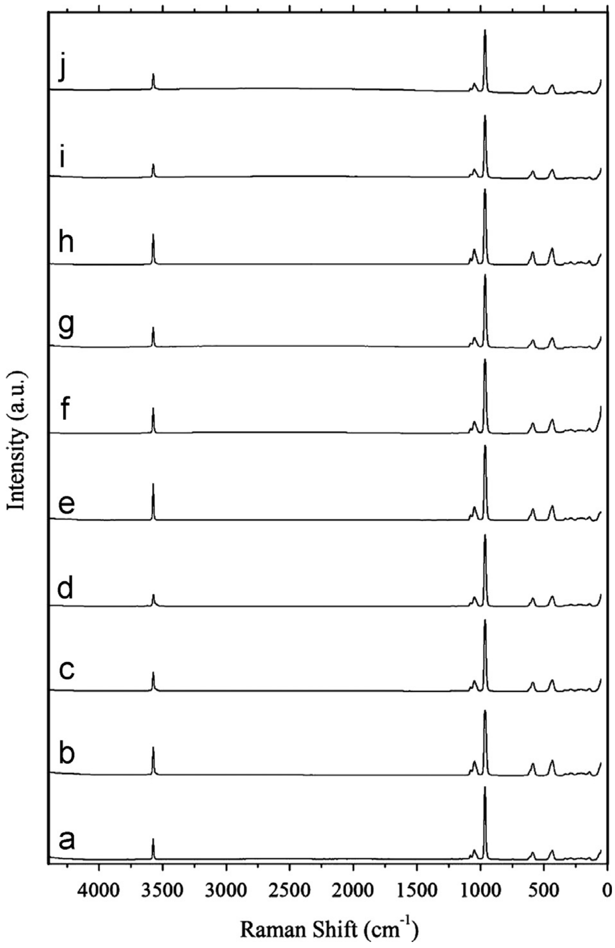

Fig. 3. Raman shift of samples sintered at 1100 °C for 1 h: (a) pure HA; (b) 1F; (c) 2F; (d) 3F; (e) 0.5Ag; (f) 1Ag; (g) 2Ag; (h) 0.5Ag1F; (i) 1Ag1F; and (j) 2Ag1F.

FTIR results of the samples sintered at 1100 °C for 1 h are shown in Fig. 2. In all of the samples, PO_4^{3-} (ν_2) bending vibration was observed at a wavelength of 474 cm^{-1}. Moreover, at wavelengths of 571 and 601 cm^{-1}, O–P–O bending mode (ν_4) in PO_4^{3-} group of HA was observed. At a wavelength of 961 cm^{-1}, symmetric stretching (ν_1) of the P–O bond in PO_4^{3-} group was observed. Furthermore, asymmetric stretching (ν_3) mode (P–O bond) of PO_4^{3-} group was observed at wavelengths of 1046 and 1090 cm^{-1}. In all of the samples, librational (ν_1) and stretching modes (ν_s) of the hydroxyl (OH$^-$) group were determined at wavelengths of 631 and 3572 cm^{-1}, respectively. In the F$^-$ doped samples (1F, 2F, 3F, 0.5Ag1F, 1Ag1F, 2Ag1F), in addition to hydroxyl group at 3572 cm^{-1}, F$^-$ band was observed at a wavelength of 3541 cm^{-1}. The bands between 1987 and 2142 cm^{-1} were related to the ν_1 and ν_3 PO_4^{3-} groups as stated previously [16]. In some of the samples (1Ag, 2Ag, 1Ag1F, and 2Ag1F), presence of ν_1 P–O stretching mode related to the TCP was observed at a wavelength of 1393 cm^{-1} as seen in Fig. 2 [16].

Raman spectroscopy results of the samples are shown in Fig. 3. In all of the samples, same Raman spectra were observed. PO_4^{3-} (ν_2) bending vibration was observed at a wavelength of 434 cm^{-1}. Moreover, at a wavelength of 588 cm^{-1}, bending mode (ν_4) in PO_4^{3-} group of HA was observed. At a wavelength of 965 cm^{-1}, symmetric stretching (ν_1) of the PO_4^{3-} group was observed. Furthermore, asymmetric stretching (ν_3) mode of PO_4^{3-} group was observed at wavelengths of 1047 and 1080 cm^{-1}. In all of the samples, stretching mode (ν_s) of the hydroxyl (OH$^-$) group was determined at a wavelength of 3578 cm^{-1}. Bands related to the presence of fluoride bands or TCP were not observed after the Raman results. This showed that FTIR results were more accurate than the Raman results in this study.

SEM images of the samples sintered at 1100 °C for 1 h are given in Fig. 4. All the samples represented equiaxed shape grains. Grain sizes calculated from these SEM images are presented in Table 2. Grain sizes of the samples were between 273 nm and 377 nm. Sample 3F and co-doped sample 0.5Ag1F had the smallest grains sizes of 273 nm and 289 nm, respectively. Small amount of co-doping resulted in small grain sizes. In a previous study, Ag doped HA showed smaller crystal size than Ag doped brushite [22].

Microhardness values for the samples sintered at 1100 °C for 1 h are shown in Table 3. Increasing the Ag$^+$ and F$^-$ ion amounts separately resulted in a continuous decrease in microhardness values of the doped samples. Although no difference was observed in microhardness values of pure and Ag doped samples in a previous study [8], increasing the Ag amount diminished the microhardness values drastically in this study. Similar to our study, increasing Ag amount in crystalline HA coating on Ti resulted in smaller microhardness values [44]. However, co-doping of Ag$^+$ and F$^-$ ions resulted in highest microhardness value for the sample of 0.5Ag1F. However, increasing the Ag$^+$ ion amount in Ag$^+$ and F$^-$ co-doped samples resulted in decrease in microhardness values.

Antibacterial activity study results of the samples against to *E. coli* are presented in Table 4. Samples of 10Ag, 5Ag1F, and 10Ag1F showed a remarkable antibacterial performance against to *E. coli*. It was previously mentioned that presence of Ag ions in HA resulted in antibacterial activity [8,14,45]. This showed that high amount of Ag$^+$ ions in HA resulted in presence of antibacterial activity.

4. Conclusions

HAs co-doped with Ag$^+$ and F$^-$ ions were synthesized by the precipitation method and sintered at 1100 °C for 1 h. Small amount of dopants in the samples resulted in high densities. In most of the samples, HA was the main phase with a small amount of β-TCP. Although Raman spectra results did not give any difference among the samples, fluoride doping and small amount of TCP were observed after the FTIR results. Samples 3F and 0.5Ag1F had the smallest grain sizes when compared with other samples. Highest microhardness value was observed for the sample co-doped with Ag$^+$ and F$^-$ ions (0.5Ag1F). High amount of Ag$^+$ ions present in HA provided antibacterial resistance to *E. coli*.

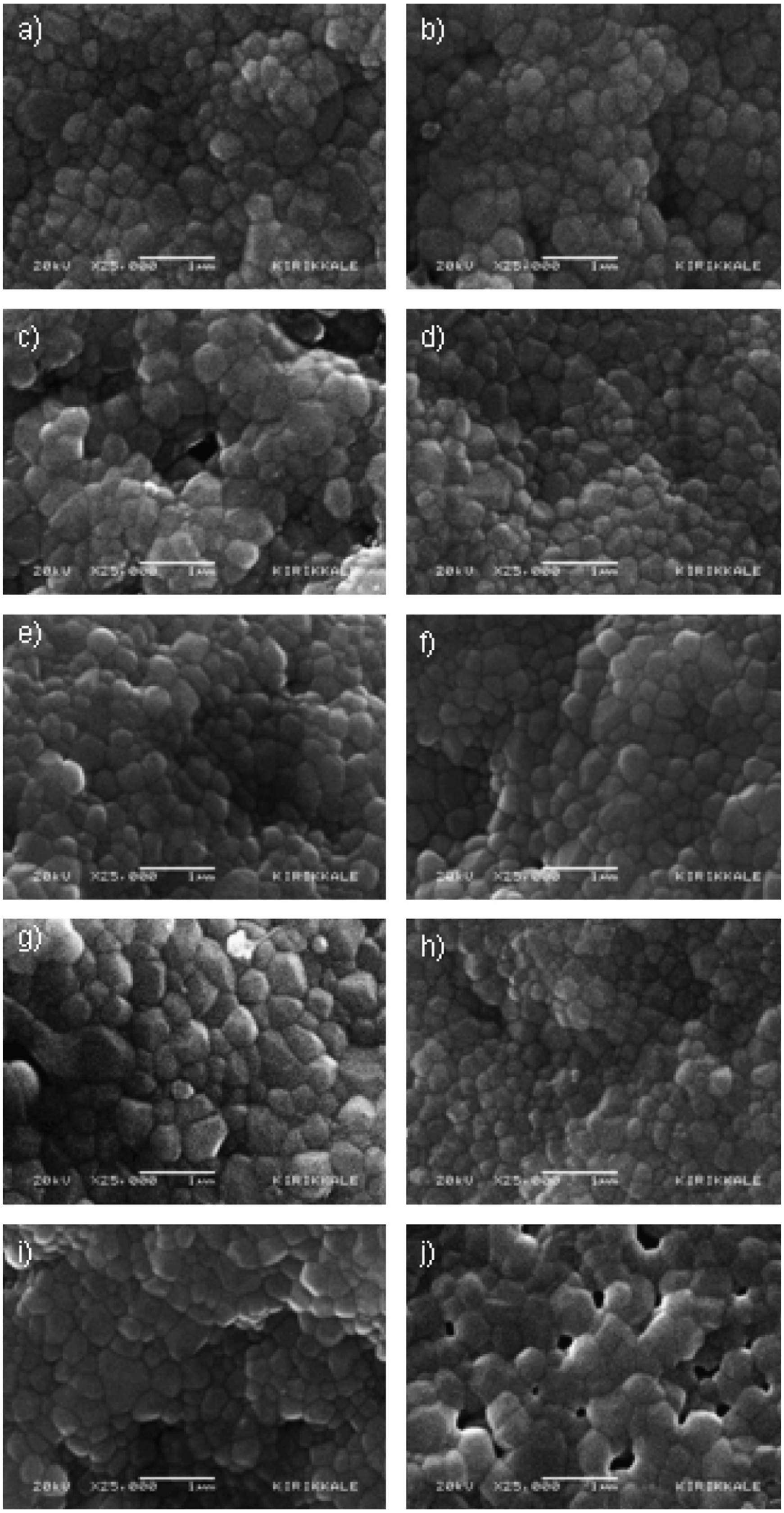

Fig. 4. SEM images of samples sintered at 1100 °C for 1 h: (a) pure HA; (b) 1F; (c) 2F; (d) 3F; (e) 0.5Ag; (f) 1Ag; (g) 2Ag; (h) 0.5Ag1F; (i) 1Ag1F; and (j) 2Ag1F.

Table 2
Grain size of the samples calculated from SEM images.

Sample ID	Particle size (nm)
Pure	300
1F	304
2F	371
3F	273
0.5Ag	377
1Ag	346
2Ag	350
0.5Ag1F	289
1Ag1F	312
2Ag1F	360

Table 3
Vickers microhardness values of the samples sintered at 1100 °C for 1 h.

Sample ID	Vickers microhardness (GPa)
Pure	5.28 ± 0.42
1F	4.88 ± 0.50
2F	4.69 ± 0.55
3F	4.61 ± 0.43
0.5Ag	5.19 ± 0.44
1Ag	4.71 ± 0.33
2Ag	4.17 ± 0.41
0.5Ag1F	6.10 ± 0.60
1Ag1F	5.26 ± 0.36
2Ag1F	2.58 ± 0.31

Table 4
Antibacterial activity of the samples against to *Escherichia coli*. (Note: (–) represents no antibacterial activity.)

Sample ID	*Escherichia coli* (cm)
Pure	–
1F	–
2F	–
3F	–
0.5Ag	–
1Ag	–
2Ag	–
5Ag	–
10Ag	2
0.5Ag1F	–
1Ag1F	–
2Ag1F	–
5Ag1F	0.9
10Ag1F	1.2

Acknowledgments

Authors would like to thank Assoc. Prof. Dr. Ozgur Ozturk from Kastamonu University for XRD analysis.

References

[1] J. Tian, Preparation of porous hydroxyapatite, Journal of Materials Science 36 (2001) 3061–3066.

[2] W. Suchanek, M. Yoshimura, Processing and properties of hydroxyapatite-based biomaterials for use as hard tissue replacement implant, Journal of Materials Research 13 (1998) 94–117.

[3] K. Ioku, G. Kawachi, S. Sasaki, H. Fujimoro, S. Goto, Hydrothermal preparation of tailored hydroxyapatite, Journal of Materials Science 41 (2006) 1341–1344.

[4] P. Laquerriere, A. Grandjean- Laquerriere, S. Addadi-Rebbah, E. Jallot, D. Laurent-Maquin, P. Frayssinet, M. Guenounou, MMP-2, MMP-9 and their inhibitors TIMP-2 and TIMP-1 production by human monocytes in vitro in the presence of different forms of hydroxyapatite particles, Biomaterials 25 (2004) 2515–2524.

[5] K. Kandori, A. Fudo, T. Ishikawa, Study on the particle texture dependence of protein adsorption by using synthetic micrometer-sized calcium hydroxyapatite particles, Colloids Surface B: Biointerfaces 24 (2002) 145–153.

[6] P. Laquerriere, A. Grandjean- Laquerriere, M. Guenounou, D. Laurent-Maquin, P. Frayssinet, M. Nardin, Correlation between sintering temperature of hydroxyapatite particles and the production of inflammatory cytokines by human monocytes, Colloids Surface B: Biointerfaces 30 (2003) 207–213.

[7] N. Bouropoulos, J. Moradian-Oldak, Analysis of hiydroxyapatite surface coverage by amelogenin nanospheres following the Langmuir model for protein adsorption, Calcified Tissue International 72 (2003) 599–603.

[8] B. Singh, A.K. Dubey, S. Kumar, N. Saha, B. Basu, R. Gupta, In vitro biocompatibility and antimicrobial activity of wet chemically prepared $Ca_{10-x}Ag_x(PO_4)_6(OH)_2$ ($0.0 \leq x \leq 0.5$) hydroxyapatites, Materials Science Engineering C 31 (2011) 1320–1329.

[9] A. Peetsch, C. Greulich, D. Braun, C. Stroetges, H. Rehage, B. Siebers, M. Köller, M. Epple, Silver-doped calcium phosphate nanoparticles: synthesis, characterization and toxic effects toward mammalian and prokaryotic cells, Colloids Surface B: Biointerfaces 102 (2013) 724–729.

[10] M. Pratap Reddy, A. Venugopal, M. Subrahmanyam, Hydroxyapatite-supported $Ag–TiO_2$ as *Escherichia coli* disinfection photocatalyst, Water Research 41 (2007) 379–386.

[11] A. Bahadir, C. Ergun, M. Baydogan, Synthesis and characterization of Ag doped hydroxylapatite as an antibacterial scaffolds material, Diffusion in Solid and Liquids IV 283–286 (2009) 250–255.

[12] D. Cayır, C. Ergun, S. Guvendik, Synthesis and characterization of Ag doped hydroxylapatite via the decomposition of EDTA chelate, Diffusion in Solid and Liquids V PTS 1 and 2 297–301 (2010) 25–29.

[13] T.N. Kim, G.L. Feng, J.O. Kim, J. Wu, H. Wang, G.C. Chen, F.Z. Cui, Antimicrobial effect of metal ions (Ag^+, Cu^{2+}, Zn^{2+}) in hydroxyapatite, Journal of Materials Science Master in Medicine 9 (1998) 129–134.

[14] H. Yang, L. Zhang, K.-W. Xu, Effect of storing on the microstructure of Ag/Cu/HA powder, Ceramics International 35 (2009) 1595–1601.

[15] V. Stanić, D. Janaćković, S. Dimitrijević, S.B. Tanasković, M. Mitrić, M.S. Pavlović, A. Krstić, D. Jovanović, S. Raičević, Synthesis of antimicrobial monophase silver-doped hydroxyapatite nanopowders for tissue engineering, Applied Surface Science 257 (2011) 4510–4518.

[16] N. Iqbal, M.R.A. Kadir, N.A.N.N. Malek, N.H. Mahmood, M.R. Murali, T. Kamarul, Rapid microwave assisted synthesis and characterization of nanosized silver-doped hydroxyapatite with antibacterials properties, Materials Letters 89 (2012) 118–122.

[17] J. Suwanprateeb, F. Thammarakcharoen, K. Wasoontararat, W. Chokevivat, P. Phanphiriya, Preparation and characterization of nanosized silver phosphate loaded hydroxyapatite by single step co-conversion process, Materials Science and Engineering C 32 (2012) 2122–2128.

[18] J.-K. Liu, X.-H. Yang, X.-G. Tian, Preparation of silver/hydroxyapatite nanocomposite spheres, Powder Technology 184 (2008) 21–24.

[19] G.A. Fielding, M. Roy, A. Bandyopadhyay, S. Bose, Antibacterial and biological characteristics of silver containing and strontium doped plasma sprayed hydroxyapatite coatings, Acta Biomaterialia 8 (2012) 3144–3152.

[20] W. Chen, Y. Liu, H.S. Courtney, M. Bettenga, C.M. Agrawal, J.D. Bumgardner, J.L. Ong, In vitro anti-bacterial and biological properties of magnetron co-sputtered silver-containing hydroxyapatite coating, Biomaterials 27 (2006) 5512–5517.

[21] N.A. Trujillo, R.A. Oldinski, H. Ma, J.D. Bryers, Antibacterial effect of silver-doped hydroxyapatite thin films sputter deposited on titanium, Materials Science and Engineering C 32 (2012) 2135–2144.

[22] A. Ewald, D. Hösel, S. Patel, L.M. Grover, J.E. Barralet, U. Gbureck, Silver-doped calcium phosphate cements with antimicrobial activity, Acta Biomaterialia 7 (2011) 4064–4070.

[23] Y.L. Lou, M.G. Botelho, B.W. Darvell, Reaction of silver daimine flouride with hydroxyapatite and protein, Journal of Dentistry 39 (2011) 612–618.

[24] R. Nirmala, K.T. Nam, D.K. Park, B. Woo-il, R. Navamathvan, H.Y. Kim, Structural, thermal, mechanical and bioactivity evaluation of silver-loaded bovine bone hydroxyapatite grafted poly (ϵ-caprolactone) nanofibers via electrospinning, Surface and Coatings Technology 205 (2010) 174–181.

[25] M. Nishioka, T. Nishimura, M. Taya, Kinetic evaluation of bactericidal activity of silver-loaded zirconium phosphate combined with hydroxyapatite in the presence of chloride ion, Biochemical Engineering Journal 20 (2004) 79–84.

[26] M. Nishioka, T. Nishimura, A. Ookubo, M. Taya, Improved bactericidal activity of silver-loaded zirconium phosphate in the presence of C^- by combining with hydroxyapatite, Biotechnology Letters 25 (2003) 1263–1266.

[27] H. Qu, M. Wei, The effect of fluoride contents in fluoridated hydroxyapatite on osteoblast behavior, Acta Biomaterialia 2 (2006) 113–119.

[28] M. Okazaki, Y. Miake, H. Tohda, T. Yanagisawa, T. Matsumoto, J. Takahashi, Functionally graded fluoridated apatites, Biomaterials 20 (1999) 1421–1426.

[29] F.C.M. Driessens, Relation between apatite solubility and anticariogenic: effect of fluoride, Nature 243 (1973) 420–421.

[30] W.J.A. Dhert, C.P.A.T. Klein, J.A. Jansen, E.A. Van Der Velde, R.C. Vriesde, P.M. Rozing, Histological and histomorphometrical investigation of fluorapatite, magnesium whitlockite, and hydroxylapatite plasma-sprayed coating in goats, Journal of Biomedical Materials Research 27 (1993) 127–138.

[31] K. Lau, C. Goodwin, M. Arias, S. Mohan, D.J. Baylink, Bone cell mitogenic action of fluoroaluminate and aluminum fluoride but not that of sodium fluoride involves upregulation of the insulin-like growth factor system, Bone 30 (2002) 705–711.

[32] J. Harrison, A.J. Melville, J.S. Forsythe, B.C. Muddle, A.O. Trounson, K.A. Gross, Sintered hydroxyfluorapatites-IV: the effect of fluoride substitutions upon colonisation of hydroyapatites by mouse embryonic stem cells, Biomaterials 25 (2004) 4977–4986.

[33] K.A. Gross, L.M. Rodriguez-Lorenzo, Sintered hydroxyfluoreapatites, Part II: mechanical properties of solid solutions determined by microindentation, Biomaterials 25 (2004) 1385–1394.

[34] R.Z. LeGeros, R. Kijowska, W. Jia, J.P. LeGereos, Fluoride-cation interactions in the formation and stability of apatites, Journal of Fluorine Chemistry 41 (1988) 53–64.

[35] K.W. Lau, K. Åkesson, C.R. Libanati, D.J. Baylink, Osteogenicactions of fluoride: its therapeutic use for established osteoporosis, in: J.F. Whitfield, P. Morley (Eds.), Anabolic Treatments for Osteoporosis, CRC Press, Boca Raton, 1998, p. 207.

[36] R. Ebrahimi-Kahrizsangi, B. Nasiri-Tabrizi, A. Chami, Characterization of single-crystal fluorapatite nanoparticles synthesized via mechanochemical method, Particuology 9 (2011) 537–544.

[37] L.M. Rodríguez-Lorenzo, J.N. Hart, K.A. Gross, Influence of fluorine in the synthesis of apatites. Synthesis of solid solutions of hydroxy-fluorapatite, Biomaterials 24 (2003) 3777–3785.

[38] A. Karlis, A.B. Kinnari, Sintered hydroxyfluorapatites. Part III: sintering and resultant mechanical properties of sintered blends of hydroxyapatite and fluorapatite, Biomaterials 25 (2004) 1395–1405.

[39] F. Ben Ayed, J. Bouaziz, K. Bouzouita, Pressureless sintering of fluorapatite under oxygen atmosphere, Journal of Europen Ceramic Society 20 (2000) 1069–1076.

[40] Z. Evis, Al^{3+} doped nano-hydroxyapatites and their sintering characteristics, Journal of Ceramic Society of Japan 114 (2006) 1001–1004.

[41] M. Jarcho, C.H. Bolen, M.B. Thomas, J. Babock, J.F. Kay, R.H. Doremus, Hydroxylapatite synthesis and characterization in dense polycrystalline form, Journal of Materials Science 11 (1976) 2027–2035.

[42] S.J. Kalita, H.A. Bhatt, Nanocrystalline hydroxyapatite doped with magnesium and zinc: synthesis and characterization, Materials Science and Engineering C 27 (2007) 837–848.

[43] N. Rameshbabu, T.S.S. Kumar, T.G. Prabhakar, V.S. Sastry, K.V.G.K. Murty, K.P. Rao, Antibacterial nanosized silver substituted hydroxyapatite: synthesis and characterization, Journal of Biomedical Materials Research 80A (2007) 581–591.

[44] M. Jelinek, T. Kocourek, J. Remsa, M. Weiserova, K. Jurek, J. Miksovsky, J. Strnad, A. Galandakova, J. Ulrichova, Antibacterial, cytotoxicity and physical properties of laser – Silver doped hydroxyapatite layers, Materials Science and Engineering C 33 (2013) 1242–1246.

[45] X. Liu, Y. Mou, S. Wu, H.C. Man, Synthesis of silver-incorporated hydroxyapatite nanocomposites for antimicrobial implant coatings, Applied Surface Science 273 (2013) 748–757.